

# Automatic Ventricular Cavity Boundary Detection from Sequential Ultrasound Images Using Simulated Annealing

N. FRIEDLAND AND D. ADAM, MEMBER, IEEE

**Abstract**—An automatic algorithm has been developed for high speed detection of cavity boundaries in sequential 2-D echocardiograms using an optimization algorithm called simulated annealing (SA). The algorithm has the following three distinct stages.

i) Image decimation: a predetermined window of size  $n \times m$  is decimated to size  $n' \times m'$  after low pass filtering.

ii) An iterative radial gradient algorithm is employed to determine the center of gravity (CG) of the cavity. A four parameter elliptical Hough transform is performed to estimate the cavity boundaries. The resulting ellipse is scaled around the CG to define an area with a high probability for the existence of the real boundary.

iii) 64 radii which originate from the CG defined in stage ii) are bounded by the high probability region. Each bounded radius is defined as a link in a 1-D, 64 member cyclic Markov random field (MRF). A highly parallel iterative stochastic relaxation optimization (SA) is performed upon the MRF. The optimization, if given sufficient time, brings an energy function to a global minimum regardless of initial conditions. This energy function, which defines a Gibbs distribution over the system, takes into consideration optimal edge detection, cavity wall smoothness, maximal cavity volume, and temporal continuity with the previous frame.

Temporal information from adjacent frames is integrated into the two parametric models to increase algorithm robustness.

This algorithm is unique in that it compounds spatial and temporal information along with a physical model in its decision rule, whereas most other algorithms base their decisions on spatial data alone. This is the first implementation of a relaxation algorithm for edge detection in echocardiograms. In view of the latter and the improved decision rule, results attained using this algorithm on real data have been highly encouraging.

## I. INTRODUCTION

ULTRASOUND imaging is more attractive, as a clinical tool, than other methods which call for exposure of the patient to high levels of nuclear or X-ray radiation. Other advantages of ultrasound imaging, besides the absence of tissue damage, are low cost, minimal discomfort, and real time processing.

Images produced by sonic methods, however, are of a relatively poor quality. Typical image degradation in-

cludes multiplicative and additive high frequency noise, blurring of spatial information perpendicular to the direction of sonic wave propagation, distortions in regions which are adjacent to the transducer, and speckle noise.

Spatial information in ultrasound pictures, due to the physical nature of the imaging system, is basically represented by speckles or blotches of relatively high gray-level intensity. These blotches can be classified into the following two groups.

*Boundary speckles*, which represent existing physical borders. These speckles can vary in size and in the distance between them.

*Random speckles*, usually smaller in size than the boundary speckles, which are imaging system artifacts and represent no real object.

The combination of these degradation effects makes the use of classical mask type FIR filters ineffective as shown by Adam *et al.* [1].

Research conducted into this problem has led to the use of more intelligent methods than the thresholded edge detector. Algorithms were developed which employed various forms of spatial information based decision rules. These algorithms, although a vast improvement on classical edge detectors, still suffer from a number of drawbacks.

Some algorithms [1]–[3] rely on human initialization and are sensitive to the selection of the interactive input. This dependence upon the subjective has two major disadvantages. First and foremost, system dependability. The quality of results attained by such an algorithm depends upon the correct selection of the initial input. There is a distinct possibility that different human operators would produce different results on the same data, through slightly different initializations. The second problem is system efficiency. Manual initialization is a time consuming and tedious task, especially when there are usually many jobs that need processing.

The second major disadvantage of the detection algorithms is the inability to cope with speckle noise, due to limited decision rules, which are based on spatial information only [1], [4], [5]. In some of the more sophisticated methods, [2] for example, temporal smoothing is implemented after the spatial decision stage. Unfortunately, such smoothing does not participate in the deci-

Manuscript received August 16, 1988; revised May 14, 1989. This work was supported in part by the Technion VPR-L and M. Kneel Heart Center Research Fund, by the Michael Kennedy-Leigh Fund, London, and by the ME Group, Woman's Division, ATS, New York.

The authors are with the Faculty of Electrical Engineering and the Department of Biomedical Engineering, Technion—Israel Institute of Technology, Haifa, Israel.

IEEE Log Number 8929506.

sion process and, therefore, is limited in its ability to correct major detection flaws.

Mailloux *et al.* [6] applied optical flow methods to ultrasound images. In this method temporal information was employed to construct the velocity field between adjacent frames. This method lacks the ability to cope with speckles that have high temporal correlation and the computation time needed to process a relatively small window area is inhibitive.

In a recent publication Chu *et al.* [7] presented an improved detection method for single frames. This method, besides the lack of temporal information in the decision making process, divides the actual detection into stages which are dealt with separately. This division in the decision process does not allow the system to realize its full potential.

In view of the objective difficulties which arise from the image degradation in ultrasound pictures, a more powerful algorithm is needed to achieve robust ventricular cavity boundary detection from a sequence of images. Such an algorithm would have to satisfy the following requirements:

- i) an improved decision rule that incorporates spatial and temporal data as well as the physical and geometrical properties of the cavity boundary;
- ii) real time processing capabilities as a basis for a clinically operational system;
- iii) automatic boundary detection to free the system from operator input dependence.

We have attempted to meet the above specifications through the implementation of an optimal optimization algorithm called simulated annealing (SA). This stochastic relaxation algorithm is especially attractive due to the following.

1) *Global Optimization*: SA, if given sufficient time, brings a smoothly varying energy function with multiple minima to its global minimum regardless of initial conditions. The energy function we will define for cavity boundary detection from ultrasonic images is of the above nature.

2) *Design Flexibility*: SA can be implemented on MRF's, which provide a great measure of freedom in energy function definition. Thus, complex decision rules can be implemented.

3) *A Highly Parallel Algorithm*: SA, when applied to MRF's, is parallelly structured, thus, parallel implementation is possible.

SA, on the other hand, suffers from two major disadvantages. The algorithm is slow when dealing with very large data arrays, as shown by Geman and Geman [8]. There is no known theory to determine the optimal energy function for a given optimization problem, therefore, energy function determination is highly heuristic.

This paper represents an algorithm for the detection of ventricular boundaries in echocardiogram and provides experimental evidence of its success, under the assumptions which are listed in Section II. We do not claim that this algorithm can be used in its present form as a general

boundary detector. We rather demonstrate its potential to make subtle decisions in a difficult domain to which it has been specifically tailored.

In Section II the algorithm is presented and the methods employed to overcome the inherent problems caused by ultrasound image degradation and the relaxation algorithm are introduced. In Section III the results of the algorithms are displayed. Section IV is a discussion of the results and of the algorithm in general.

## II. METHODS AND PROCEDURE

### A. Assumptions

In the development of the following algorithm we have made several general assumptions about the geometrical properties of the cavities in question as well as the behavior of the digitized data in the spatial and temporal domains.

- The ventricular cavity can be roughly approximated by an upright ellipse at all stages of the cardiac cycle. This assumption does not impose a serious limitation upon the problem because it is only an initial estimate.
- First degree neighborhoods are sufficient to describe the cavity boundary dynamics using the MRF representation. The purpose of this is to limit the extent of computations needed at each site in the MRF. Our results substantiate this claim.
- Spatial information is confined mainly to the lower frequency bands, therefore, low pass filtering and decimation does not greatly reduce the quality of the data. This may be untrue in images which have clearly defined boundaries in them, but since this is obviously not the case here, it is a safe assumption to make.
- Temporally consecutive video rate frames display small changes in cavity boundary location. This is obvious from comparing video rates to the rates of change in the monitored process.

### B. Input Picture Decimation

The ultrasound images are recorded and stored in a video format. The video images are sampled by a Vicom image processor, and stored as a  $512 \times 512$  pixel array with 8 bit gray-level resolution. In order to reduce computation time, a region of interest is defined and a spatial decimation is performed.

In this stage the region undergoes low pass filtering to enable a  $4:1 \times 4:1$  decimation to be implemented without an aliasing effect. Spatial definition is preserved due to the fact that relevant information is maintained in the low frequency areas. The filtering process employs a  $7 \times 7$  FIR LPF which is tabulated over a 2-D Hamming window.

### C. "High Probability" Zone Definition

1) *Initialization*: The algorithm is initialized by inserting a cursor into the desired cavity in the first frame of the sequence. This is the only human interactive input that this algorithm needs in the detection process.

2) *Primary Detection—The Elliptic Model*: The objective of the primary detection is to provide a very general approximation of the boundary location. The general shape approximation elected for use was the ellipse, because geometrically ellipses are flexible enough to roughly describe all configurations of ventricular cavities in echocardiographs. On the other hand, the analytical elliptical model is simple enough to be matched quickly using a four parameter equation

$$\frac{(x - x_0)^2}{a^2} + \frac{(y - y_0)^2}{b^2} = 1 \quad (1)$$

where  $x_0, y_0$  are the Cartesian coordinates of the ellipse's center of gravity and  $a, b$  are the half values of the ellipse's major axes in the  $x, y$  directions.

One of the most successful methods of matching analytical geometric models to given data in pictures is known as the Hough transform. An example of how this is done for ellipses is given by Ballard [9]. Unfortunately, model matching using four parameters is both demanding in storage space and time consuming. An adaptation was needed to efficiently employ the Hough transform in this algorithm. Thus, the elliptical model is matched to the decimated data picture in the following two stages.

i)  $x_0, y_0$  are determined by the star algorithm.

ii)  $a$  is determined using a 1-D Hough transform based upon the final configuration of the star algorithm.  $b$  is determined by averaging the final configuration and the value found for  $a$ .

i) *The Star Algorithm*: The star algorithm, which determines  $x_0, y_0$  is defined by the following procedure.

(a) Determine an initial position inside the required cavity  $i_{cg}^0, j_{cg}^0$  in the first frame of the sequence. (If this is not the first frame of the sequence, the initial point will be taken as  $i_{cg}^{final}, j_{cg}^{final}$  of the previous frame.)

(b) Using  $i_{cg}^0, j_{cg}^0$  as the origin, project  $N$  radii which are angularly equispaced by  $\Delta\theta = (2\pi/N)$ .

(c) Perform a thresholded optimal<sup>1</sup> step edge detection process along each radii, using

$$F_{edge}(r^i) = \frac{1}{3} \{ x(r^i + 2) + x(r^i + 1) + x(r^i) - x(r^i - 1) - x(r^i - 2) - x(r^i - 3) \} \quad (2)$$

where  $r^i$  is a given radial increment upon radius  $i, i \in 1, 2, \dots, N$ .  $x(r)$  represents the local gray-level values in the decimated picture along the different radii. If the filter output value along a radius  $i$  is greater than the threshold  $edge_{thr}$  stop progressing along radius  $i$  and go on to radius  $i + 1$  until all  $N$  radii have been processed. The resulting  $N$  stop points are retained.

<sup>1</sup>This filter is optimal in the sense that it produces a maximum signal-to-noise ratio while minimizing the distance from the peak in the output to the actual edge location. The input data have already undergone low pass filtering and the operator width is small, thus, the probability of multiple responses is attenuated. Therefore, this simple filter is equivalent to Canny's [10] with respect to edge detection and localization, while less expensive to implement.

(d) Using the  $N$  stop points attained in (c) calculate the new center of gravity  $i_{cg}^1, j_{cg}^1$ .

(e) Repeat (b)–(d) until

$$\{ (i_{cg}^{k+1} - i_{cg}^k)^2 + (j_{cg}^{k+1} - j_{cg}^k)^2 \}^{1/2} < c_{g_{thr}}.$$

The output reached at convergence  $i_{cg}^{final}, j_{cg}^{final}$  is the elliptic models' centroid coordinates  $x_0, y_0$ . The final configuration radial stop values are used in the next stage of the primary detection, i.e., the determination of  $a$  and  $b$ .

ii) *Determining  $a$  and  $b$  Using a 1-D Hough Transform*: The first step is to define a search range for the possible values of  $a$  and  $b$ . Next, a 1-D accumulator is constructed, with appropriate slots for every value of  $a$  in the search range. The initial values of the accumulator are set to zero. For  $x_0, y_0$  and for each point  $x, y$  of the final  $N$  radial values around  $x_0, y_0$ , all determined by the final configuration of the star algorithm, and for every value of  $b$  in a predetermined search range, that maintains

$$b^2 > (y - y_0)^2 \quad (3)$$

calculate  $a$  by

$$a = \left\{ \frac{(x - x_0)^2}{1 - \frac{(y - y_0)^2}{b^2}} \right\}^{1/2} \quad (4)$$

and increment the corresponding  $a$  value slot in the accumulator by 1. After  $a$  has been calculated for all values of  $x, y$ , and  $b$ , the accumulator is searched for a maximum value. This value becomes  $\hat{a}$  and is used to calculate  $\hat{b}$  by

$$\hat{b} = \frac{1}{N} \sum_{x,y} \left\{ \frac{(y - y_0)^2}{1 - \frac{(x - x_0)^2}{\hat{a}^2}} \right\}^{1/2}. \quad (5)$$

Due to the distribution of the final radii, the elliptic model has one distinct maximum value. Therefore, the use of a 1-D accumulator does not limit the output possibilities and a savings of time and storage is achieved.

3) *Determining the "High Probability" Zone*: Once a rough approximation of the cavity boundary has been made, the system has to be prepared for the optimization by defining the 1-D, cyclic MRF. This MRF's sites are composed of  $N$  random variables which represent possible boundary locations in radial coordinates. In order to reduce the load of computations we have determined a "high probability" zone, which hedges the values that each radial site can attain in the course of the optimization. These upper and lower bounds on the radial values  $r_{LB}^i, r_{UB}^i$  are separately calculated for all  $i \in \{1, 2, \dots, N\}$ . Since the MRF is centered around the  $x_0, y_0$  which are the centroid of the elliptic model, the bounds have been attained through scaling the model ellipse by  $S_{LB}, S_{UB}$  and taking the intersection points of the resulting ellipses and the radii to be the upper and lower bounds.

This zone allows the powerful optimization process to concentrate on an area which has a high probability for real boundary existence. In order to ensure this the scaling parameters have to be large enough, otherwise large de-

tection errors will result. The correct scaling will, however, effectively reduce the data size and computation time with no error penalty, i.e., a scaling must be large enough to include the entire boundary required, yet as small as possible to minimize the load.

An example of the primary detection and the "high probability" zone results are depicted in Fig. 1. The empirical values of the appropriate scaling factors are listed in Table I of Section III.

#### D. Data Reduction Summary

The first two stages of the algorithm perform an intelligent data reduction upon the original input image. The global decimation of stage 1 causes a reduction ratio of 16:1. The primary detection and definition of the "high probability" zone implements a further reduction due to the transition to bounded polar coordinates. The overall data reduction ratio of the system going into the global optimization is therefore approximately 250:1, given a  $512 \times 512$  input picture and taking  $N$  as 64.

#### E. Simulated Annealing, The Global Optimization

In order to implement the optimization using simulated annealing several stages must be performed:

- i) energy function definition;
- ii) annealing schedule definition;
- iii) iterative optimization through state transitions.

The basic algorithm used here is similar to that used by Geman and Geman [8] for improving noisy images. Geman and Geman defined a 2-D MRF which, due to its size, is far from being real time oriented. This algorithm defines the bounded radii which were created in the early stages as an  $N = 64$  member, cyclic, 1-D MRF. Thus, a very significant savings in computation time and storage is achieved. This algorithm maintains the positive qualities of SA, while suppressing the principal drawbacks, mainly the long execution time.

1) *Optimization System Definitions:* Let  $X = \{x_1, \dots, x_N\}$  be a vector of discrete random variables  $x_i$  which represents the  $N$  possible radial values that the system can attain and let  $r = \{r^1, r^2, \dots, r^N\}$  represent a possible configuration of radii values, where  $r^i$  is a radial value between  $r_{LB}^i$  and  $r_{UB}^i$  and  $N$  is the number of radii.

Let  $R$  be the set of all possible configurations, so that  $r \in R$ . Then  $X$  is an MRF if

$$P(X = r) > 0 \quad \forall r \in R \quad (6)$$

and

$$\begin{aligned} P(x_i = r^i | x_j = r^j; j \neq i) \\ = P(x_i = r^i | x_j = r^j; j \in Ne_i) \\ \forall i \in \{1, 2, \dots, N\} \text{ and } r \in R \end{aligned} \quad (7)$$

where  $Ne_i$  is a neighborhood of  $x_i$ . In this algorithm the neighborhood is defined as the two nearest radial elements so that  $Ne_i = \{i - 1, i + 1\}$ .

Let  $U(r)$  represent an energy function defined over the configuration space  $R$ , so that for every event  $\{X = r\}$ ,

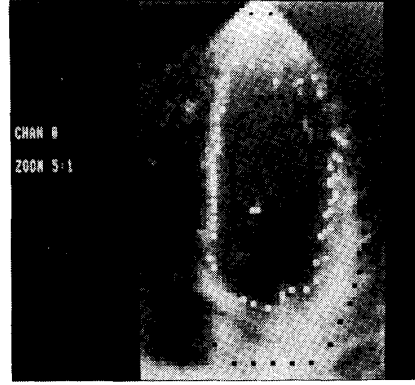


Fig. 1. This picture depicts the final star algorithm radii value configuration (white points) upon the  $4:1 \times 4:1$  decimated region of interest, enlarged five times. Black points represent the upper and lower radial values of the "high probability" zone. The zone is defined by scaling the parametric ellipse calculated by the adapted 1-D Hough transform. Notice that the zone distinctly envelopes the real boundary despite the fact that final star algorithm radii values were "stuck" in the cavity interior and "escaped" through holes in the cavities boundaries.

$U(r)$  attains a given value depending upon the energy function definition. The Gibbs distribution of this system, therefore, is defined as

$$\pi(r) \triangleq \frac{1}{Z} e^{-U(r)/T_k} \quad (8)$$

where  $T_k$  is a given temperature value and can be regarded in the meantime as a constant, and  $Z$  is the partition function and is defined as follows:

$$Z \triangleq \sum_r e^{-U(r)/T_k} \quad (9)$$

It was shown elsewhere [8] that the existence of a Gibbs distribution and an MRF over a given system is equivalent. Therefore, the energy function  $U(r)$  defines both the physical properties of the desired optimization and the MRF itself. SA, which equivalently brings the energy function to its global minimum or brings the MRF to its most probable state, is highly sensitive to the selection of the energy function. Energy function selection is, at present, highly heuristic, and theoretical means of determining an optimal energy function for a given problem are still lacking.

2) *Energy Function Selection:* Energy function elements can be categorized into two basic groups: "magnetic field" (MF) type elements, which operate independently on each MRF site  $x_i$ ,  $i \in \{1, 2, \dots, N\}$ ; and "electric field" (EF) type elements, which operate through neighbor interaction only upon the defined neighborhood  $Ne_i$  around  $x_i$ .

The type names have an historical meaning which dates back to the Ising model [11]. The analog scheme [8] calls for energy function structure that is similar to that of the "two field" concept.

As mentioned above, energy function selection is highly heuristic and the optimization is highly sensitive to the

correct definition of  $U(r)$ . On the other hand, the lack of direct dependence between the optimization process and the energy function in use enables a great measure of freedom in decision rule design. In this specific case of ultrasound image cavity boundary detection, the energy function or decision rule implemented consists of the following four elements:

- a) optimal edge detection along each of the radii (MF type);
- b) radial value smoothness between neighboring radii (EF type);
- c) maximization of cavity volume (MF type);
- d) temporal continuity with the previous frame (EF type).

This type of optimization is known as a "frustration" problem because the participating elements may work in a difference of interests, thus, the resulting solution is the best compromise given the energy function and the data.

a) *The Optimal Edge Detector Element*: This energy function element employs a filter which is equivalent to the Canny [10] step edge detector. This filter was employed in the star algorithm and was defined in (2). As explained earlier, the equivalence to the Canny detector is mainly due to the fact that the data have already undergone low pass filtering and that the filter size is small, thus, multiple responses are attenuated.

$$U_1 = \begin{cases} (F_{edge}(r^i) + 1)^{-1} & \text{if } F_{edge}(r^i) > 0 \\ |F_{edge}(r^i) + 1| & \text{if } F_{edge}(r^i) \leq 0. \end{cases} \quad (10)$$

The  $U_1$  function is designed to be biased towards discovering positive edges, as the ventricle interior tends to be of lower gray-level intensity. It also has the property of quickly "pushing" the boundary outwards while the radial value is still in the ventricle's interior by assigning very high values to  $U_1$ .

b) *The Radial Smoothness Element*: This element takes into consideration the fact that the ventricular boundary is continuous and therefore large variations in neighboring radial values are not likely to occur. The smoothness condition helps to prevent boundary errors due to dominant random speckles in the cavity interior. The neighborhood system employed is the two nearest radii  $\{r^{i-1}, r^{i+1}\}$ :

$$U_2 = \frac{|r^{i+1} - r^i| + |r^{i-1} - r^i|}{2r^i}. \quad (11)$$

c) *The Maximum Volume Element*: This element assists the detection process in disregarding secondary boundaries which can be caused by internal muscle movement and valve fluctuations. The maximization "pushes" the boundary to the cavity walls where the dominant optimal edge detector element counters the expansion

$$U_3 = \frac{1}{1 + (r^i - r_{LB}^i)} \quad (12)$$

where  $r_{LB}^i$  is the lower bound of the "high probability" zone on radial vector  $r^i$ . This function was specifically

designed to yield a normalized worst case configuration. Other functions may be selected, but this one has shown good results.

d) *The Temporal Continuity Element*: Temporal continuity can be extremely useful in sequential detection, especially if the information in adjacent frames does not vary greatly. This element minimizes the difference between the present boundary conversion and the previous one, which is translated to the appropriate radial values in the new coordinate system

$$U_4 = \frac{|r_t^i - r_{t-1}^i|}{r_t^i} \quad (13)$$

where  $r_t^i$  is the radial value for the present frame (in time  $t$ ) and  $r_{t-1}^i$  is the convergence value of the detection algorithm from the previous frame translated to the coordinate system of the cavity centroid in this frame. Only one temporal neighbor is utilized, the  $r_{t-2}^i$  neighbor was not used because of the possible errors that could be caused by large temporal variation in an image sequence. This element, although awarded a relatively small weight value due to the above, still contributed significantly in the local distributions of the modified Gibbs sampler [see Section II-E-4-a)], thus, highly upgrading the overall results. Comparative results attained while setting  $\alpha_4$  to zero were distinctly inferior.

e) *Combining the Energy Function Elements*: After the different elements have been selected and given functional structure, a linear combination is performed to "weld" them into a single unit. This unit then defines the Gibbs distribution over the optimization problem and the simulated annealing algorithm can be implemented. The general form of the linear combination is

$$U = \alpha_1 \times U_1 + \alpha_2 \times U_2 + \alpha_3 \times U_3 + \alpha_4 \times U_4 \quad (14)$$

where  $\alpha_i$  are constants.

The constants' values are determined empirically after the elements functional structures have been selected. This process is performed by initially considering all elements to be independent. A successful weight is found while all others are kept constant. This is repeated until a satisfactory configuration is attained over a test set of input data.

3) *Determining the Annealing Schedule*: Due to the fact that the 1-D, cyclic, MRF is of finite length, the algorithm, according to Aarts and van Laarhoven [12], is of the inhomogeneous type. Thus, the temperature series employed is critical for algorithm convergence and the following condition must be met:

$$T_k \geq \frac{c}{\log(1 + k)} \quad (15)$$

where  $c$  is the annealing schedule constant,  $k$  is the iteration index, performed over the MRF.

Hajek [13] showed that to ensure algorithm convergence,  $c$  had to be greater or equal to the largest "cup" in the energy state space. A "cup" is defined as the dif-

ference between the minimal energy value needed to exit a group of states in the systems' configuration state space and the minimum energy value attained in that group.

This type of solution, despite the fact that it ensures global convergence theoretically, is difficult to implement because it calls for a complete analysis of the energy state space. We elected therefore to determine the  $c$  constant empirically, where two considerations were taken into account.

1) If the value of  $c$  is too small, the optimization may not converge to a global minimum.

2) If the value of  $c$  is too large, the optimization will not be practical due to the many iterations needed before the temperature  $T_k$  has reached a low enough value.

4) *The Iterative Optimization and Configuration Transition:* After the annealing schedule constant  $c$  and the total number of iterations " $n_a$ " have been determined, the optimization is performed. The algorithm, in each iteration, sequentially visits all members of the 1-D MRF, i.e., all the radii, and attempts a configuration transition at each member. The transition is divided into the following two parts.

i) The local Gibbs distribution is sampled ("Gibbs sampler") and a new radial value is offered.

ii) The new radial value is tested to determine whether it is acceptable.

After each complete sweep of all the MRF members, the temperature parameter  $T_k$  is reduced in accordance with the annealing schedule. This process is repeated until " $n_{it}$ " iterations have been completed. The resulting configuration at the conclusion of this process is at a global minimum upon the energy function.

a) *The Modified Gibbs Sampler:* The Gibbs sampler developed by Geman and Geman [8] was adapted to the present algorithm. The purpose of the modified Gibbs sampler is to increase algorithm efficiency by sampling new configurations which are of relatively high occurrence probability. These configurations are attained in the sequential implementation by running a radial site between its extremum values while freezing the neighborhood configuration. Each radial value results in a different energy value. These values are used to readjust the discrete probability distribution of the random variable which corresponds with that site in the MRF. This site is then sampled, generating the next candidate configuration of the MRF. This process is sitewise independent due to the MRF and is the main motivation to seek in future parallel processing protocols for this algorithm.

The local formulation of the sampler, given the Gibbs distribution as presented in (8), is

$$f_{gibbs}^k(\omega_i^r) = \frac{\exp\left\{\frac{-U(\omega_i^r)}{T_k}\right\}}{\sum_{x=r_{LB}}^{r_{UB}} \exp\left\{\frac{-U(\omega_i^x)}{T_k}\right\}} \quad (16)$$

$\omega_i^r, \omega_i^x \in \mathbf{R}$  are configurations where the only changes are radial values  $r$  and " $x$ " at the radius  $i$ .  $f_{gibbs}^k(\omega_i^r)$  repre-

sents the samplers discrete distribution for the radius  $i$  and iteration  $k$ .

Thus,  $r_k^i$ , the new radial value of the  $i$ th radius in the  $k$ th iteration, is sampled and a new candidate system configuration  $\eta$  is generated.

b) *Transition Acceptance:* Now that a new configuration  $\eta$  has been generated, the algorithm tests the effect it has upon the system. SA differs from other optimization schemes in that it accepts changes which increase the value of the energy function. Thus, it is able to escape local minima.

Let  $\eta$  be a new configuration received from the Gibbs sampler. The new value for the energy function is calculated:  $U(\eta)$ , let the old value be  $U(r_{k-1})$  and we define  $\Delta U$  as

$$\Delta U \triangleq U(r_{k-1}) - U(\eta) \quad (17)$$

where  $r_{k-1}$  represents the old configuration value.

Next a parameter " $q$ " is defined

$$q \triangleq \exp\left\{\frac{-\Delta U}{T_k}\right\}. \quad (18)$$

The acceptance process is as follows:

1) if  $\Delta U > 0$ , then  $r_k = \eta$ ;

2) if  $\Delta U \leq 0$ , then sample  $0 \leq \gamma \leq 1$  (uniformly distributed)

$$r_k = \begin{cases} \eta & \text{if } \gamma \leq q \\ r_{k-1} & \text{if } \gamma > q. \end{cases} \quad (19)$$

Notice that for high temperature values  $q \rightarrow 1$ , most of the state transitions are accepted. As  $T_k \rightarrow 0$ ,  $q \rightarrow 0$  and very few transitions are accepted. The results of the optimal radii configuration are depicted in Fig. 2.

5) *Temporal Smoothing of the Data Pictures:* Temporal smoothing was performed on the data before the two major detection stages, i.e., the "high probability" zone definition and the SA global optimization.

The purpose of the smoothing in both cases is to increase algorithm robustness. In both cases data from the immediate neighbors at  $\{t-1, t+1\}$  were employed.

In the "high probability" zone definition stage the Hough transform was performed, taking into consideration the final points received from three frames, after a center of gravity position correlation test was conducted. The test ensures that neighboring pictures whose spatial information varies greatly from the frame in question, do not participate in the smoothing process. This is done by checking the position of the center of gravity in the neighboring frames and calculating the shift in the temporal dimension. Frames whose shift values are large are discarded in the smoothing.

In the optimization stage the resulting bounded radial values of the "high probability" zone are smoothed with the corresponding pixel values in the neighboring frames that passed the shift test. This smoothing eliminates high frequency noise and random interior speckles with low time correlation.

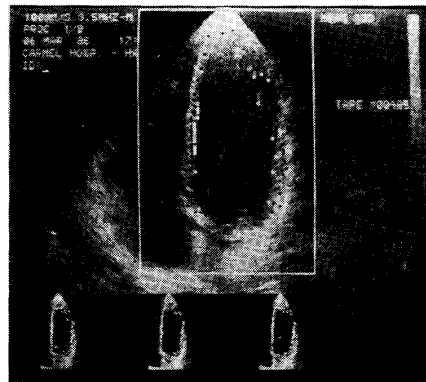


Fig. 2. This picture depicts the final global optimization configuration (black points) given the Canny edge detector initialization configuration (white points) upon the region of interest (white box). Three decimated images, which compound the data for the time sequence  $\{t-1, t+1\}$ , appear at the bottom from left to right. The "high probability" zone and the star algorithms final radii values are superimposed on each one. To the right of the decimated images is the output of the optimal edge detector in the "high probability" zone along each of the radii. The maximum output value positions of the Canny FIR filter are marked in white.

TABLE I  
EMPIRICAL CONSTANTS' VALUES

Constant	Stage	Description	Value	Sensitivity
$LPC_{size}$	preprocessing	low pass filter size	$7 \times 7$	1
$df$	preprocessing	decimation factor	4:1	1
$N$	zone definition	number of radii	64	2
$Edge_{thr}$	star algorithm	edge detector threshold	15	2
$cg_{thr}$	star algorithm	( $cg$ ) threshold	1.5	1
$S_{LB}$	zone definition	lower bound scaling parameter	0.7	2
$S_{UB}$	zone definition	upper bound scaling parameter	1.6	2
$c$	SA optimization	annealing schedule constant	0.1	2
$n_{it}$	SA optimization	number of optimization iterations	200	2
$\alpha_1$	SA optimization	energy function constant	1.0	3
$\alpha_2$	SA optimization	energy function constant	1.4	3
$\alpha_3$	SA optimization	energy function constant	0.5	3
$\alpha_4$	SA optimization	energy function constant	0.1	3

Sensitivity—1: insensitive 2: sensitive 3: very sensitive

### III. RESULTS

This section presents results attained by applying the SA algorithm on real data images. The processing was performed on a Digital Equipment Corporation VAX 11/750. Typical processing time for a single picture was approximately 90 s with the relaxation algorithm implemented sequentially. In Table I the selected algorithm empirical constants' values have been tabulated. Different values were examined for each constant over a wide range. The combination of values given in Table I represents the best results attained through value variations of  $\pm 10$  percent.

The preprocessing stage was implemented in order to reduce the dimensions of the data matrix. A 4:1 decimation was performed along each axis, therefore, to pre-

vent aliasing effects the image was convolved with a  $7 \times 7$  low pass filter. The parameter  $N$ , which represents the number of radii, was taken as 64. This number provides a reasonable distance between the radii endpoints so that boundary continuity can be examined without putting too much importance on a single radial value [2]. This also ensures that the radii are spaced far enough apart that the probability of more than one of them hitting a noise speckle is small. The edge detector threshold,  $Edge_{thr}$ , was generated by checking the histograms of an ensemble of decimated images. The  $cg_{thr}$  was taken as a measure of convergence for the star algorithm. The accuracy of these thresholds does not need to be great because the star algorithm only generates a very poor approximation of the cavity contour which is greatly refined by the optimization. The zone definition parameters were determined by

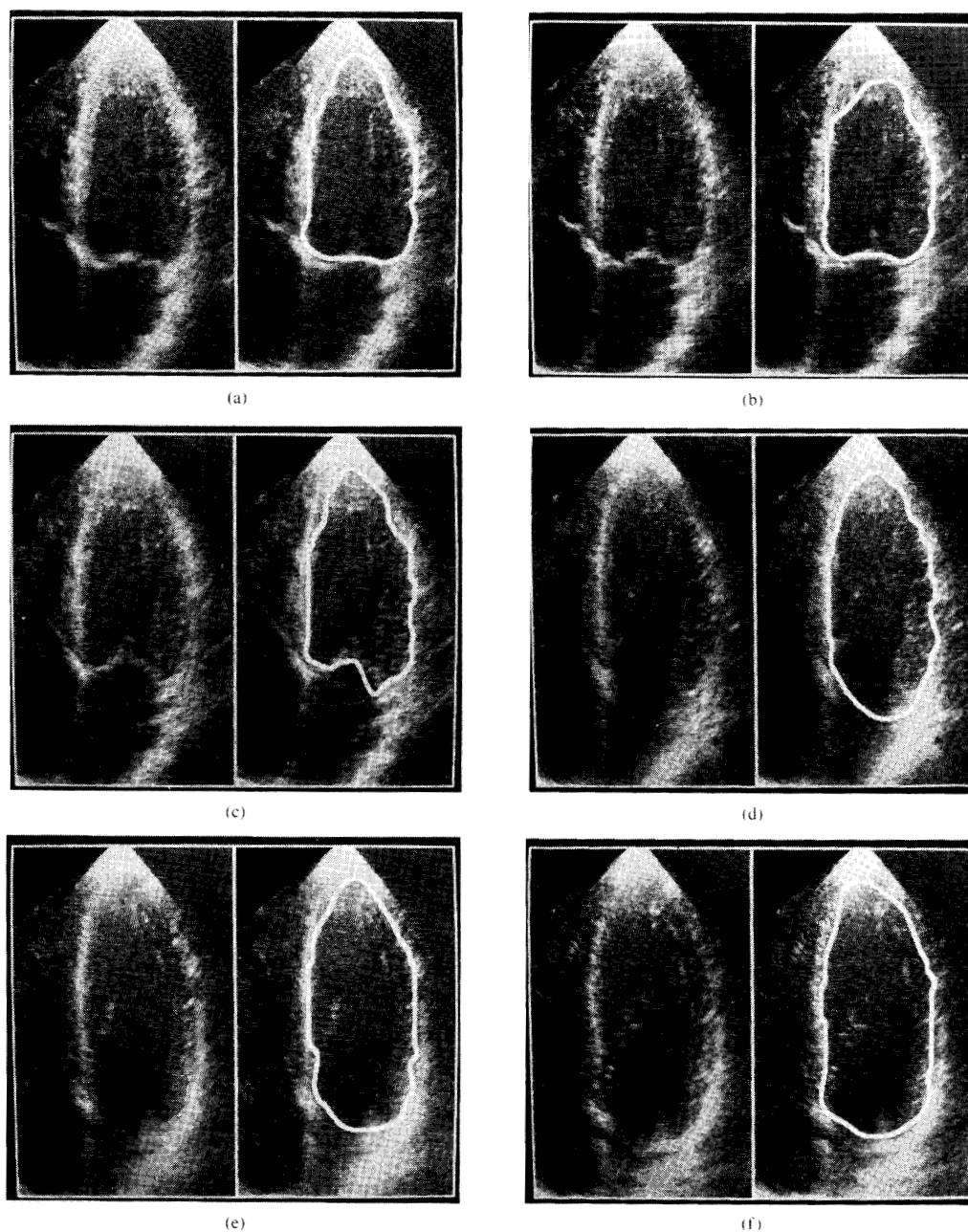


Fig. 3. Simulated annealing optimization results. The pictures (a)–(k) depicted in this figure, represent the algorithm convergence values at different stages of a given cycle. The left side presents the original data in a  $200 \times 300$  pixel region of interest. The right side presents the same data, with the algorithm's convergence radii configuration joined by a B-Spline algorithm, superimposed upon it. (a) Systolic stage. (b) End systolic. (c) Initial diastolic, valve opening. (d) Diastolic stage. (e) Diastolic stage. (f) Diastolic stage. (g) Diastolic stage. (h) End diastolic. (i) Initial systolic. (j) Systolic stage, secondary border detected at bottom due to valve movement. (k) Systolic stage.

examining the extreme fluctuations in the ventricular shape and adding a safety factor to that. It is advantageous to reduce the size of the zone because this represents a

large reduction in the amount of calculations made during the optimization. On the other hand this zone must maintain its character: mainly to define along each of the radii



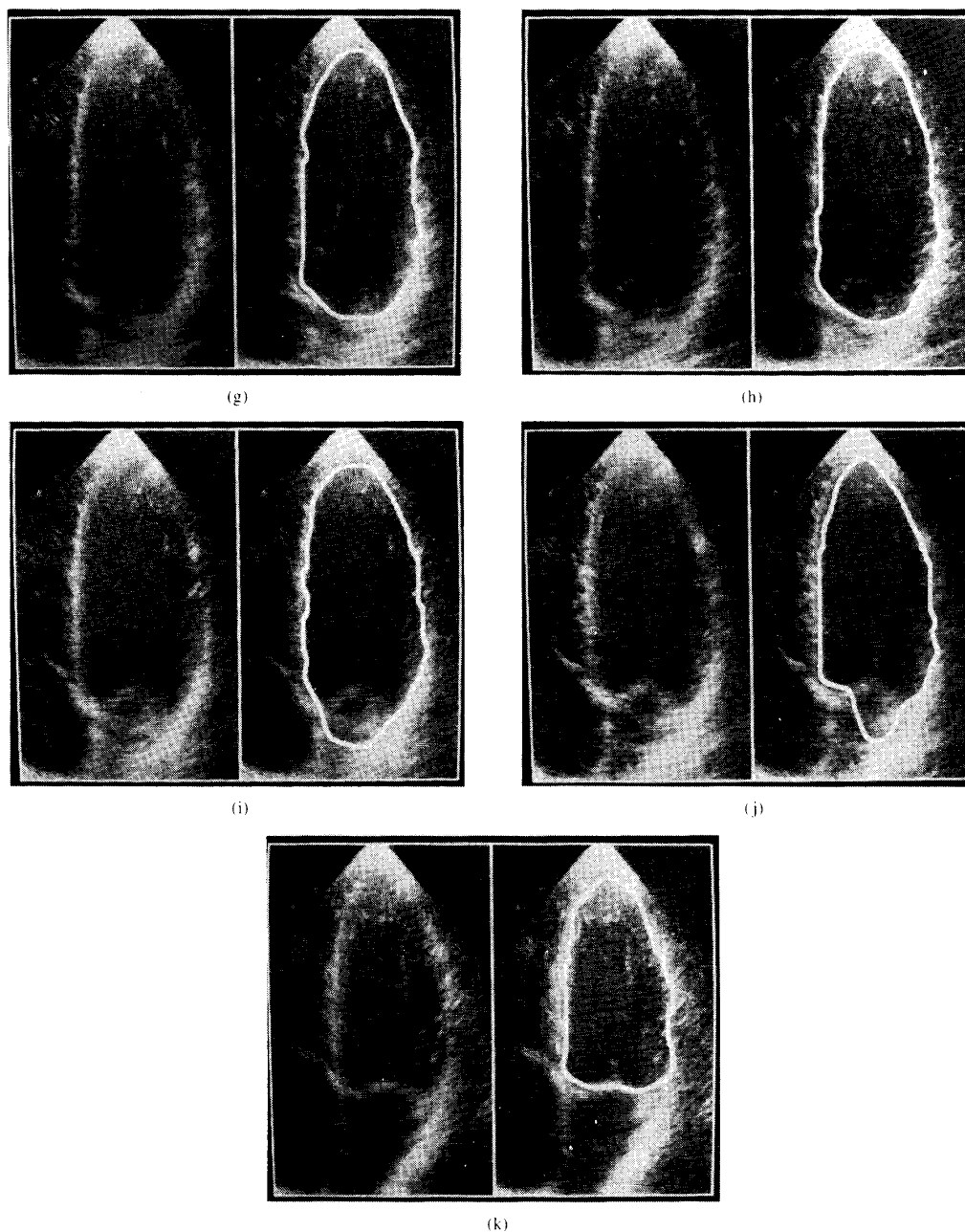


Fig. 3. (Continued.)

the extremum values of the optimization search. Care must be taken that the real boundary always exists in this zone or else large errors will occur. The SA optimization parameters were defined in a hands-on trial and error procedure. They represent the most problematic aspects of the algorithm. The convergence rate must be slow enough to allow the relaxation to converge to a global minimum, but fast enough to be reasonably implemented in a working system. The weight parameters had to be fine tuned over a large group of test data, and the results are most

sensitive to their definition. The encouraging fact was that once these parameters were correctly established the algorithm provided correct results for a large collection of image sequences which were processed with it. Thus, to the extent that those images were representative of echocardiograms, this technique is a robust sequential boundary detector for this application.

The results of the algorithm on real data have been arranged in Fig. 3. The optimization convergence points were joined using a B-Spline algorithm and superimposed

on the original data. The original image appears on the left and the algorithm results on the right, to allow the reader an objective comparison.

In Fig. 3 a sequence of 11 images taken approximately 50 ms apart is presented. In this sequence picture (b) is at end systol and picture (h) at end diastol, thus, the entire span of myocardial ventricular shapes is given. In this sequence it is evident that the endocardial edges at the free wall and the septum are clearly detected. In some of the pictures where the mitral valve is open, and thus the local edge does not exist, the algorithm selected a boundary which most complied with its decision rule. This local boundary selection does not undermine the correct endocardial border detection in other areas of the ventricle. The algorithm performs markedly well in the epical zone where there are heavy image distortions due to the proximity of the transducer. The improved decision rule achieves a high rate of success in detecting very poorly defined edges, as seen in pictures (f) and (g). The results presented in Fig. 3 demonstrate the potential of the SA based algorithm and its robustness.

#### IV. DISCUSSION

In this paper we have attempted to address a boundary detection problem in a very difficult domain, echocardiography. It is this domain which has made the design of an automatic algorithm using classic image processing methods inadequate. A new approach to the problem is needed. We believe that the ideas presented in this paper may contribute to the wider use of ultrasound in cardiac imaging as the clinical tool of choice. The increased use of this imaging modality versus other imaging modalities will not only reduce costs but will be painless and cause no tissue damage from high energy radiation.

The novelty of this algorithm is the implementation of the simulated annealing optimization method in detecting ultrasound image cavity boundaries from a sequence of input images. Although the global minimum may theoretically not be found in finite time using SA, our experience with this problem shows satisfactory convergence with relatively inexpensive computational cost, even for a sequential implementation. This convergence of the state space into a high probability configuration was achieved regardless of initial conditions. Thus, credibility was maintained by ensuring a unique solution for every data set. SA also allowed the utilization of an MRF which yields design flexibility in the selection of a heuristic decision rule. This rule, which is a unique feature of this algorithm, took into account a number of physical and geometrical properties of echocardiographic cavities from sequential input images. All of the energy function elements simultaneously participated in the determination of

the boundary points' location. It was this approach which freed the system from interactive operator dependence.

SA was efficiently implemented by employing global image decimation and a primary detection stage. The data were reduced by a 250:1 ratio. Thus, a 64 member 1-D, cyclic, MRF was defined instead of a 2-D,  $512 \times 512$  MRF. Computation time, using the small MRF, was kept at approximately 90 s/frame for sequential implementation. Due to the parallel nature of the SA algorithm when applied to MRF's, independent parallel processing for each of the 64 radii will reduce computation time even further. Hence, it is shown that this algorithm has the potential to be implemented in real time.

The algorithm attained a high level of success in overcoming speckle effects. Boundary speckles were joined into a continuous cavity border and random speckles were ignored in the detection. The algorithm also ignored secondary boundaries caused by internal muscle movement. Detection problems occurred in the base area of the ventricle, where valve opening caused the algorithm to define a border according to its decision rule.

There is no comprehensive theory which defines the optimal energy function for a given optimization problem. Despite this fact, the suboptimal results attained by this method have a high success rate and show great promise for on-line implementation.

#### REFERENCES

- [1] D. Adam, O. Hareuveni, and S. Sideman, "Semiautomatic border tracking of cine echocardiogram ventricular images," *IEEE Trans. Med. Imaging*, vol. MI-6, pp. 266-271, Sept. 1987.
- [2] L. Zhang and E. A. Geiser, "An effective algorithm for extracting serial endocardial borders from 2-D echocardiograms," *IEEE Trans. Biomed. Eng.*, vol. BME-31, pp. 441-447, June 1984.
- [3] R. S. Prasad and T. M. Srinivasan, "An image method for cardiac motion analysis," *IEEE Trans. Biomed. Eng.*, vol. BME-34, pp. 244-247, Mar. 1987.
- [4] E. J. Delp *et al.*, "The analysis of 2-D echocardiograms using a time varying approach," *IEEE Comput. Cardiol.*, pp. 391-394, 1982.
- [5] E. Garcia *et al.*, "Automated computer enhancement and analysis of LV 2-D echocardiograms," *IEEE Comput. Cardiol.*, pp. 399-402, 1982.
- [6] G. E. Mailloux, A. Bleau, and R. Petitclerc, "Computer analysis of heart motion from 2-D echocardiograms," *IEEE Trans. Biomed. Eng.*, vol. BME-34, pp. 356-364, May 1987.
- [7] C. H. Chu, E. J. Delp, and A. J. Buda, "Detecting left ventricular endocardial and epicardial boundaries by digital two-dimensional echocardiography," *IEEE Trans. Med. Imaging*, vol. MI-7, pp. 81-90, June 1988.
- [8] S. Geman and D. Geman, "Stochastic relaxation, Gibbs distribution, and the Bayesian restoration of images," *IEEE Trans. Pattern Anal. Machine Intell.*, vol. PAMI-6, pp. 721-741, 1984.
- [9] D. H. Ballard, "Generalizing the Hough transform to detect arbitrary shapes," *Pattern Recognition*, vol. 12, pp. 123-137, 1981.
- [10] J. Canny, "A computational approach to edge detection," *IEEE Trans. Pattern Anal. Machine Intell.*, vol. PAMI-8, pp. 679-698, 1986.
- [11] E. Ising, *Zeitschrift Physik*, vol. 31, p. 253, 1925.
- [12] P. J. M. van Laarhoven and E. H. L. Aarts, *Simulated Annealing: Theory & Applications*. Dordrecht, The Netherlands: Reidel, 1987.
- [13] B. Hajek, "Cooling schedules for optimal annealing," *Math. Operations Research*, 1986.